Interpretation of bound states in inhomogeneous superconductors: the role of Andreev reflection

1996 J. Phys.: Condens. Matter 8 169

(http://iopscience.iop.org/0953-8984/8/2/006)

J. Phys.: Condens. Matter **8** (1996) 169–191. Printed in the UK

Interpretation of bound states in inhomogeneous superconductors: the role of Andreev reflection

Ondřej Šipr†‡ and Balázs L Györffy†

† H H Wills Physics Laboratory, University of Bristol, Tyndall Avenue, Bristol BS8 1TL, UK
‡ Institute of Physics of the Academy of Sciences of the Czech Republic, Cukrovarnická 10, 162 00 Praha 6, Czech Republic

Received 30 June 1995, in final form 10 November 1995

Abstract. We study the quasiparticle bound states of superconductor–normal-metal–superconductor (S–N–S) junctions using the framework of Bogoliubov–de Gennes equations. We find that whilst the frequently employed semiclassical approximations give a good account of the overall spectra, a rich variety of interesting details get lost in making such simplifications. In particular, this is the case with the behaviour of states corresponding to large momenta parallel to the interfacial planes and with bound states above the gap. We compare the spectra of the S–N–S junction with an analogous non-superconducting semiconductor–metal–semiconductor system and show how the new features can be understood in simple physical terms. We also examine the limitations of using Andreev reflection alone to describe the trapping of normal-state quasiparticles inside normal regions embedded in a superconductor.

1. Introduction

As has been known for a long time, inhomogeneities in the pairing potential $\Delta(\boldsymbol{r})$ of a superconductor can give rise to bound quasiparticle states—in a manner similar to binding by a 'normal' $U(\boldsymbol{r})$-potential. Such bound states have been found theoretically in superconducting films deposited on normal metals (de Gennes and Saint-James 1963), in the core of a vortex line (Caroli *et al* 1964), in superconductor–normal-metal–superconductor structures (Andreev 1966, Kulik 1969), and in other systems as well. Furthermore, the contribution of the bound states is essential, e.g., for Josephson currents in mesoscopic weak links (Bardeen and Johnson 1972, Furusaki and Tsukada 1991), for tunnelling densities of states and current–voltage characteristics of films with superconducting surface sheaths (Kümmel 1977, Entin-Wohlman and Bar-Sagi 1978) and for the differential conductance as measured by a scanning tunnelling microscope near the vortex cores of type-II superconductors (Shore *et al* 1989, Gygi and Schlüter 1991). The role played by bound states in the transport properties of superconducting mesoscopic weak links was recently analysed by Martín-Rodero *et al* (1994) and Levy Yeyati *et al* (1995), and superconducting ballistic point contacts were investigated by Hurd and Wendin (1994).

The Andreev reflection of quasiparticles at the normal-metal–superconductor boundary (Andreev 1964) has been identified as the key phenomenon underlying the existence of these bound states. However, as was noted first by Kümmel (1974), not all the bound states in inhomogeneous superconductors can be generated in this way. Moreover, most of the previous calculations involving bound states employed the so-called 'Andreev' or 'semiclassical' approximation (Andreev 1964, Bardeen *et al* 1969), which is not suited

0953-8984/96/020169+23$19.50

for investigation of quasiparticles moving rapidly in the direction parallel to the normal-metal–superconductor interface (alternatively, in exact formulations, the movement in that direction was suppressed altogether (Gygi and Schlüter 1991)).

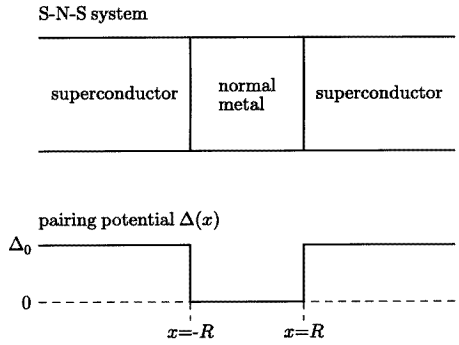

Figure 1. Schematic cross-sections of the tri-layer S–N–S system investigated in this paper. The normal $U(x)$-potential is zero everywhere; the thickness of the normal middle layer is $2R$. The system is uniform in the Y- and Z-directions.

In this paper, we wish to throw some light on some interesting features of these bound states. We shall go beyond the semiclassical arguments of Andreev (1964) and Bardeen *et al* (1969), dispense with the simplification of Gygi and Schlüter (1991) and investigate some basic features of the bound states generated by a well in the pairing potential $\Delta(\boldsymbol{r})$, using *exact* solutions of the full Bogoliubov–de Gennes (BdG) equations. To make headway, we concentrate on the simplest case of all—a slab-like square well in $\Delta(\boldsymbol{r})$, as depicted in figure 1. Previous calculations demonstrated that such a $\Delta(\boldsymbol{r})$ is a good approximation to the full self-consistent solution of the BdG equations for a superconductor–normal-metal–superconductor (S–N–S) system (Plehn *et al* 1991, Hara *et al* 1993, Plehn *et al* 1994). As we shall be concerned only with some qualitative features of the spectra, we believe that our main results can be transferred to other geometries as well (e.g. to cylindrical vortices).

The scope of our paper is as follows. First, in section 2, a summary of the theoretical framework is given. We present particular solutions of the BdG equations for the system under investigation and discuss their properties for various values of relevant quantum numbers. In section 3, the bound-states energy spectrum is investigated. We present our results, obtained using exact solutions of the BdG equations, and compare them with the outcomes of various approximate calculations. Also, an intuitive interpretation of the bound states based on comparing energy spectra of an S–N–S system and of a semiconductor–normal-metal–semiconductor (Sm–N–Sm) system is suggested. The densities of states are presented and analysed in section 4 and a brief comment on the experimental observability of the novel features is made. Finally, the role of the Andreev reflection and of other scattering processes of quasiparticles at a normal-metal–superconductor (N–S) interface are investigated in section 5.

2. Bogoliubov–de Gennes equations for an S–N–S system and their solutions

For clarity, in this section, we want to recall the basic equations that we relied upon and give a brief outline of the methods that we employed in solving them yielding the results presented in the following sections.

Bogoliubov–de Gennes (BdG) equations for the quasiparticle amplitudes $u(\boldsymbol{r})$ and $v(\boldsymbol{r})$ proved to provide a very efficient, fully microscopic framework for investigating inhomogeneous superconductors. We write them in their basic form (de Gennes 1966)

$$\begin{aligned}&[-\nabla^2 - \mu + U(\boldsymbol{r})]u(\boldsymbol{r}) + \Delta(\boldsymbol{r})v(\boldsymbol{r}) = Eu(\boldsymbol{r})\\ &-[-\nabla^2 - \mu + U(\boldsymbol{r})]v(\boldsymbol{r}) + \Delta^*(\boldsymbol{r})u(\boldsymbol{r}) = Ev(\boldsymbol{r})\end{aligned} \tag{1}$$

where $U(\boldsymbol{r})$ is the normal one-electron potential, $\Delta(\boldsymbol{r})$ is the pairing potential and μ is the chemical potential of the system under study. Rydberg atomic units ($\hbar = 1$, $e^2 = 2$, $m = 1/2$) are used in equation (1). In order to solve system (1) for a plane geometry, i.e. in the case where the potentials $U(\boldsymbol{r})$ and $\Delta(\boldsymbol{r})$ are non-uniform in the X-direction only, we separate the variables x, y and z by setting

$$u(\boldsymbol{r}) = u(x)\frac{1}{2\pi}\exp[\mathrm{i}(k_y y + k_z z)] \qquad v(\boldsymbol{r}) = v(x)\frac{1}{2\pi}\exp[\mathrm{i}(k_y y + k_z z)]. \tag{2}$$

Furthermore, to improve the transparency, we drop the normal $U(x)$-potential by setting $U(x) = 0$ in what follows. The pairing potential $\Delta(\boldsymbol{r})$ is taken to be real and of the form (cf. figure 1)

$$\Delta(x) = 0 \Leftrightarrow |x| < R \qquad \Delta(x) = \Delta_0 \Leftrightarrow |x| > R.$$

Then, the 'one-dimensional' wave-functions $u(x)$, $v(x)$ satisfy the equations

$$\begin{aligned}&\frac{\mathrm{d}^2}{\mathrm{d}x^2}u(x) + [\mu_t + E]u(x) - \Delta(x)v(x) = 0\\ &\frac{\mathrm{d}^2}{\mathrm{d}x^2}v(x) + [\mu_t - E]v(x) + \Delta(x)u(x) = 0.\end{aligned} \tag{3}$$

The new variable

$$\mu_t \equiv \mu - \left(k_y^2 + k_z^2\right) \tag{4}$$

introduced in equation (3) plays the role of an 'effective chemical potential'. It acquires its largest value $\mu_t = \mu$ when the magnitude of the parallel component of the wave-vector, $t = \sqrt{(k_y^2 + k_z^2)}$, is zero. That would correspond to a truly one-dimensional case. If we are dealing with a three-dimensional slab-like geometry, however, t can take any value between zero and infinity, implying that the domain of definition of μ_t is actually $\mu_t \in (-\infty; \mu)$. Allowing μ_t to acquire values over the full range of its definition, and particularly also to be negative, will lead us to investigate features beyond the reach of the semiclassical approximation.

The solutions of a one-dimensional BdG equation (3) for a piecewise-constant potential are constructed in such a way that, first, fundamental systems of solutions for in the host and in the spacer regions are found separately, and then they are matched across the interface so that both the wave-functions $u(x)$, $v(x)$ and their first derivatives $u'(x)$, $v'(x)$ remain continuous. As the whole problem possesses a mirror symmetry with respect to the $x = 0$ plane, even- ($\ell = 0$) and odd- ($\ell = 1$) parity solutions can be searched for separately. This means that only one of the two interfaces at $x = -R$ and at $x = R$ has to be taken into account (see Butler (1976) for a thorough analysis of the analogy between the planar and the spherical symmetry). In the normal region ($|x| < R$), solutions of the system of equations (3) can be written in terms of spinor functions:

$$\hat{\psi}_1^{(N)} = \begin{pmatrix}1\\0\end{pmatrix}\exp(\pm\mathrm{i}\gamma_1 x) \qquad \hat{\psi}_2^{(N)} = \begin{pmatrix}0\\1\end{pmatrix}\exp(\pm\mathrm{i}\gamma_2 x) \tag{5}$$

where the frequencies γ_1, γ_2 are

$$\gamma_1 = \sqrt{\mu_t + E} \qquad \gamma_2 = \sqrt{\mu_t - E}. \tag{6}$$

In the superconducting region ($|x| > L/2$), the solutions are

$$\hat{\psi}_1^{(S)} = \begin{pmatrix} u_0 \\ v_0 \end{pmatrix} \exp(\pm \mathrm{i}\omega_1 x) \qquad \hat{\psi}_2^{(S)} = \begin{pmatrix} v_0 \\ u_0 \end{pmatrix} \exp(\pm \mathrm{i}\omega_2 x) \tag{7}$$

where

$$u_0 = E + \Delta_0 + \sqrt{E^2 - \Delta_0^2} \qquad v_0 = E + \Delta_0 - \sqrt{E^2 - \Delta_0^2} \tag{8}$$

the frequencies ω_1, ω_2 being

$$\omega_1 = \sqrt{\mu_t + \sqrt{E^2 - \Delta_0^2}} \qquad \omega_2 = \sqrt{\mu_t - \sqrt{E^2 - \Delta_0^2}}. \tag{9}$$

Depending on the values of the effective chemical potential μ_t and of the excitation energy E, the normal-state frequencies γ_1, γ_2 can either be real or purely imaginary, while the 'superconducting' frequencies ω_1, ω_2 can be real, purely imaginary or complex. Evidently which of these alternatives is the case has a crucial importance for the number of spinor wave-functions, which form the fundamental system in the normal-state region and in the superconducting region, for a particular choice of the continuous 'quantum numbers' μ_t and E.

A detailed summary of the situation concerning the number of functions in the fundamental system of BdG equations (3) is presented in figure 2. In the normal (middle) region, one does not need to care about the normalizability; however, the wave-functions have to be constructed so as to be either even ($\ell = 0$) or odd ($\ell = 1$). This implies that just two linearly independent solutions are available in the fundamental system of equations (3) for $|x| < R$, no matter whether both γ_1 and γ_2 are imaginary (region B_{norm} in the '(μ_t,E)-plane'), or γ_1 is real and γ_2 is imaginary (region C_{norm}), or both γ_1 and γ_2 are real (region D_{norm})—see figure 2(*a*). In the superconducting region, those wave-functions which diverge exponentially at $x = -\infty$ or at $x = \infty$ have to be rejected (the choice of ℓ does not pose a constraint now). That means that the number of normalizable solutions is two in the regions A_{sup} (frequencies ω_1 and ω_2 are complex) and B_{sup} (both ω_1 and ω_2 are imaginary), three in the region C_{sup} (ω_1 is real and ω_2 is imaginary) and four in the region D_{sup} (both ω_1 and ω_2 are real). Note that the curve separating the region C_{sup} from the rest of the (μ_t,E)-plane conforms to $E = \sqrt{({\mu_t}^2 + \Delta_0^2)}$ (cf. equation (9)).

The complete set of solutions constructed in this way can be formed exclusively by real functions. The matching conditions at the superconducting–normal-region interface give rise to a set of four linear algebraical equations. Hence, discrete bound states can occur in the A_{sup}- and the B_{sup}-regions (the eigen-energy spectrum is determined by condition that the secular determinant is zero), while continuum states exist at any point of the C_{sup}- and D_{sup}-regions of the (μ_t,E)-plane (see figure 2(*b*)). Obviously, the discrete states are bound (i.e. decaying) only in the X-direction (perpendicular to the interface), while their wave-functions extend to infinity in the parallel-to-the-interface direction—cf. equation (2).

Note that our analysis reveals the possibility that discrete bound states exist also for excitation energies *larger* than the gap, Δ_0. Such states are analogous to the case of particles confined to a slab-like potential well in the normal $U(x)$-potential. Clearly, within the semiclassical approximation which assumes that $\mu_t > 0$ (Andreev 1966, Bar-Sagi and Kuper 1974, Plehn *et al* 1991), one cannot investigate bound states with $E > \Delta_0$ (cf. figure 2). Thus, we will pay special attention to this interesting case.

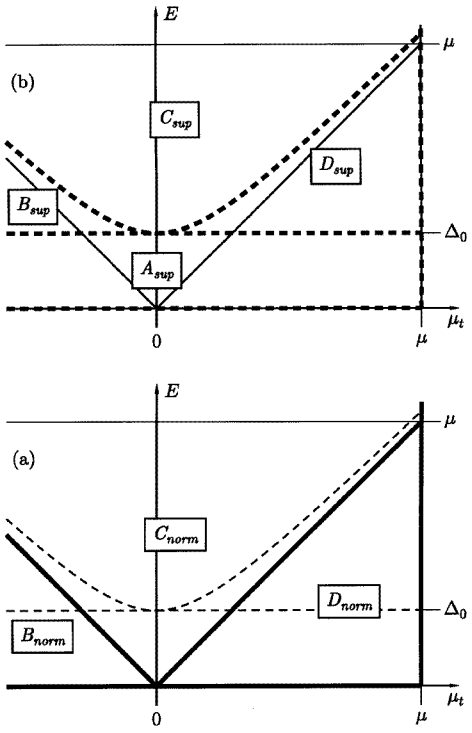

Figure 2. Division of the (μ_t, E)-plane into individual regions in the normal (a) and superconducting (b) layer. The boundaries concerning the normal layer are shown with solid lines while the boundaries relevant to the superconducting layers are shown with broken lines. In the normal case, the C_{norm}-region is separated from the B_{norm}- and D_{norm}-regions by straight lines, $E = |\mu_t|$. In the superconducting case, the region C_{sup} is marked by the curve $E = \sqrt{(\mu_t{}^2 + \Delta_0^2)}$. Note that the region A_{sup}, which spans the whole section below the $E = \Delta_0$ straight line in (b), has no counterpart in the normal case.

3. The excitation energy spectrum

In this section, the eigen-energy curves $E_{\ell n}(\mu_t)$ will be presented for both parities, $\ell = 0$ and $\ell = 1$ (the quantum number n distinguishes between energy levels corresponding to the same ℓ and μ_t). We will then compare them to the $E_n(\mu_t)$-curves which follow from the semiclassical approximation; they are expected to agree for large enough μ_t. For small μ_t, exact $E_{\ell n}(\mu_t)$-curves will be compared with the approximative analytical formula of Kümmel (1974), as this is expected to give better agreement than the semiclassical approximation in this μ_t-range. Finally, in section 3.3, we present an intuitive interpretation of the bound states based on the analysis of their spectra.

Throughout this section (as well as throughout sections 4 and 5), we measure the energy in units of the Fermi energy E_{F} and the distances in units of the inverse Fermi wave-vector k_{F}^{-1}. The particular system for which all the calculations presented here were done (see figure 1) is determined by the numerical values

$$\Delta_0 = 0.05E_{\mathrm{F}} \qquad R = 3\xi_0 \qquad \mu = 1.0E_{\mathrm{F}} \tag{10}$$

(ξ_0 is the usual Bardeen–Cooper–Schrieffer (BCS) coherence length, which is $\xi_0 = 2/(\pi\Delta_0)$ in our units). We have checked that the general features of our results do not depend on

the particular choice of the values in equation (10).

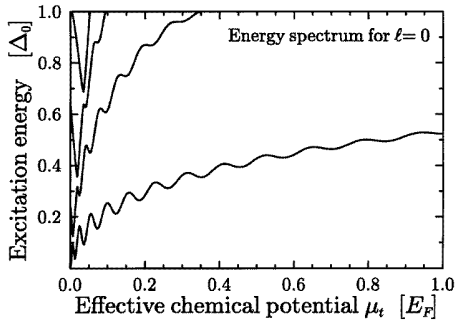

Figure 3. The energy excitation spectrum of bound even-parity states ($\ell = 0$) in an S–N–S junction for the effective chemical potential range $0 < \mu_t < \mu = 1.0E_F$.

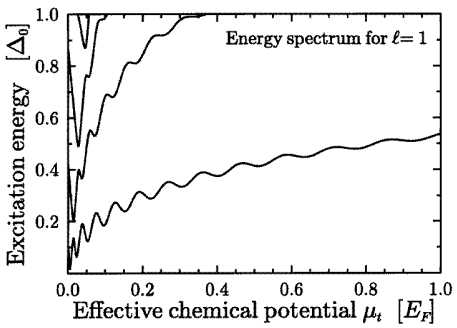

Figure 4. The energy excitation spectrum of bound odd-parity states ($\ell = 1$) in an S–N–S junction for $0 < \mu_t < \mu = 1.0E_F$.

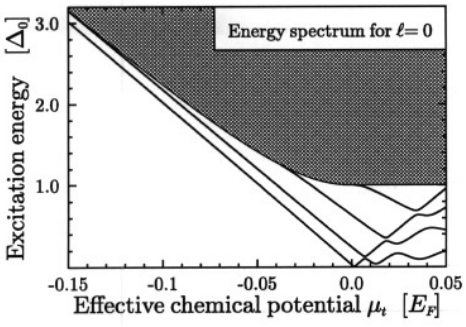

Figure 5. The energy excitation spectrum of bound even-parity states ($\ell = 0$) in an S–N–S junction for $-0.15E_F < \mu_t < 0.05E_F$. Note that bound states with excitation energies above the gap are present. The hatched part of the plot denotes the region where only oscillatory states can exist.

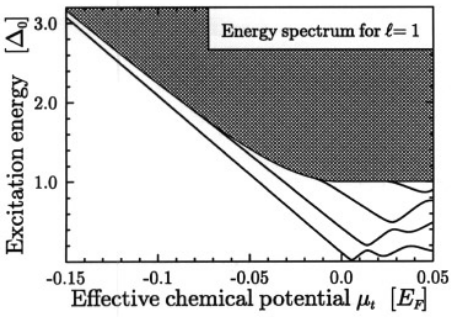

Figure 6. The energy excitation spectrum of bound odd-parity states ($\ell = 1$) in an S–N–S junction for $-0.15E_F < \mu_t < 0.05E_F$. As in figure 5, the hatched part of the plot denotes the region where only oscillatory states can exist.

3.1. Exact eigenvalue spectra of the Bogoliubov–de Gennes equations for a slab

For each parity ℓ, the excitation eigen-energy spectral curves $E_{\ell n}(\mu_t)$ were found by searching for the zeros of the secular determinant numerically. The results are presented for two partially overlapping ranges of μ_t in figures 3–6. In total, four 'energy bands' emerged for each ℓ. These bands oscillate with μ_t (for $\mu_t > 0$ only) and do not cross each other: although a local minimum of an upper band occurs approximately for the same μ_t as a local maximum of a lower one, there is always a small 'minigap' left between any two bands.

Considering results of a semiclassical analysis (Gunsenheimer *et al* 1994), we can deduce that when the bound states merge into the continuum-states region (see figure 2), they change to quasi-bound resonance states.

As noted in section 2, the range of μ_t is actually $\mu_t \in (-\infty; \mu)$. For $\ell = 1$, the lowest-energy band merges into the continuum region $C_{\rm sup}$ at $\mu_t = -0.75416E_{\rm F}$, $E = 0.75581E_{\rm F}$ (i.e. at $E = 15.116\Delta_0$). For $\ell = 0$, the lowest energy band has not merged the $C_{\rm sup}$ continuum region within the investigated μ_t-interval (which has stretched down to $\mu_t = -6E_{\rm F}$). The question of whether this band would disappear for negative μ_t even larger in absolute value or whether there would exist at least one bound state for any μ_t has remained open.

It is worth noting that we have not found any bound states in the $B_{\rm norm}$-region of the (μ_t,E)-plane, i.e. for $\mu_t < -E$, although the general analysis of section 2 does not exclude such a possibility. We will address this issue later in section 5.3.

Another remarkable feature, not inferable from figures 3–6, is that whenever either the depth of the well Δ_0 or its width $2R$ increases, the number of energy bands rises and the minigaps between them decrease at the same time. We have found that this trend is a general one.

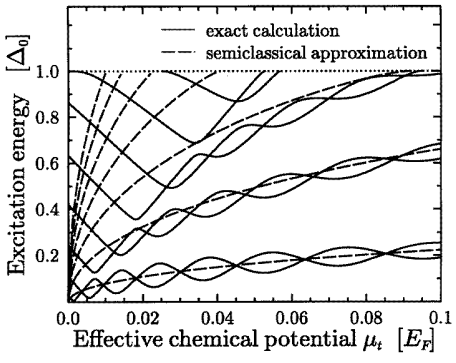

Figure 7. A comparison of bound-states excitation energy spectra obtained employing exact solutions of BdG equations (solid lines, both $\ell = 0$ and $\ell = 1$ symmetries plotted together) and employing the semiclassical approximation (broken lines) for $0 < \mu_t < 0.1E_{\rm F}$. Only the first seven 'semiclassical' bands are shown.

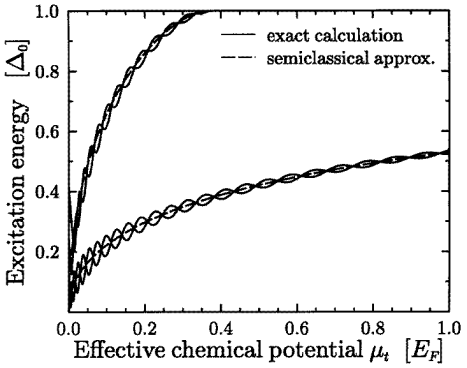

Figure 8. A comparison of bound-states excitation energy spectra obtained within an exact calculation (solid lines, both $\ell = 0$ and $\ell = 1$ symmetries plotted together) and within the semiclassical approximation (broken lines) for $0 < \mu_t < \mu = 1.0E_{\rm F}$. Only the two bands lowest in energy are displayed.

3.2. Comparison with other calculations

The semiclassical, Andreev or WKBJ approximation is the one most frequently used in investigating S–N–S junctions. Basically, it consists in writing the quasiparticle amplitudes in the form (Andreev 1964, Bar-Sagi and Kuper 1974)

$$\begin{pmatrix} u(x) \\ v(x) \end{pmatrix} = \begin{pmatrix} \bar{u}(x) \\ \bar{v}(x) \end{pmatrix} \exp(\mathrm{i}k_{\rm F}x) \tag{11}$$

and neglecting the Laplacian of $\bar{u}$ and $\bar{v}$ with respect to $k_{\rm F}\nabla$ (a thorough discussion of various formulations of the semiclassical approximation can be found, e.g., in Kobes and Whitehead (1987) or Ashida *et al* (1989)). Within this approximation, the eigen-energies for the system depicted in figure 1 satisfy the equation (Kulik 1969, Furusaki and Tsukada

1991, Plehn *et al* 1991)

$$\arccos\left(\frac{E_n}{\Delta_0}\right) - \frac{E_n R}{\sqrt{\mu_t}} = -n\pi \qquad n = 0, 1, 2, \ldots. \tag{12}$$

Energy eigenvalues based on equation (12) were presented in Bar-Sagi and Kuper (1974), Plehn *et al* (1991) or in Gunsenheimer *et al* (1994). For the particular system under study (see the beginning of section 2), the energy spectra obtained within an exact-solutions framework (figures 3–6) and within the semiclassical approximation (equation (12)) are compared in figures 7–8 for two ranges of μ_t. Note that exact results for both $\ell = 0$ and $\ell = 1$ are presented in each of the figures simultaneously. Figure 7 shows that, as expected (Kümmel 1974), the semiclassical theory does not provide a good description of bound-states eigen-energies for small μ_t. Nevertheless, it describes fairly accurately the overall behaviour of the $E_{\ell n}(\mu_t)$-curves for larger μ_t, as demonstrated in figure 8 for the two lowest energy bands. Evidently, the most significant difference between the semiclassical and the exact energy eigenvalues is the absence of oscillations in the former. Moreover, the semiclassical energy bands are 'degenerate' with respect to ℓ and appear to represent an average of the two exact curves.

As noted earlier in the end of section 2, states with $\mu_t < 0$ cannot be dealt with within the semiclassical framework.

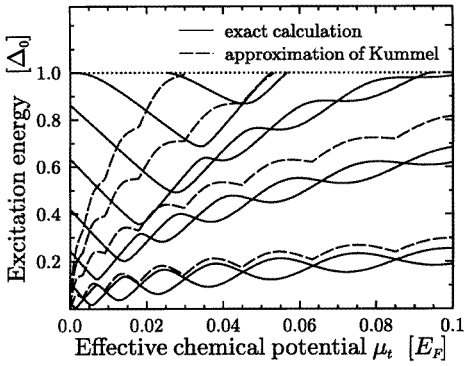

Figure 9. A comparison of the bound-states excitation energy spectra obtained by solving the BdG equations exactly (solid lines, both $\ell = 0$ and $\ell = 1$ symmetries plotted together) and by using the approximative formula of Kümmel (1974) (broken line).

Kümmel (1974) was probably the first one to stress a different character of bound quasiparticle states with small μ_t. He presented approximative analytical expressions (equations (3.1)–(3.2) in Kümmel (1974) and equation (2.6) in Kümmel (1977)) describing energy levels of low-lying bound states with small μ_t. In figure 9, we compare the exact energy bands with those evaluated using expressions of Kümmel (1974) for our particular system (when using relevant equations of Kümmel (1977), the overall picture remains the same). It is evident that Kümmel's formula describes well the 'upper' branch of the lowest energy band. However, it does not take into account the splitting of the band due to the quantum number ℓ. For higher E, the agreement is less satisfactory, which is not surprising as the approximative formula was derived on condition that $E \ll \Delta_0$ (Kümmel 1974, 1977).

3.3. Intuitive interpretation of the bound states

The physical mechanism responsible for bound-states formation in S–N–S junctions was identified as the Andreev reflection of quasiparticles at an N–S interface (Andreev 1966): the states bound by potential wells in the pairing $\Delta(x)$-potential are basically standing waves of Andreev-reflected particles and holes. However, such an explanation does not offer a comprehensive intuitive insight into the phenomenon—it deals solely with the 'mechanism of confinement' of quasiparticles in the middle normal region. Moreover, as noted already by Kümmel (1974), not all bound states below the gap can be generated by the Andreev reflection. We will investigate the role of the Andreev reflection and of other related processes at N–S interfaces in detail in section 5. Here, we want to focus on presenting an alternative view of the mechanism of bound-states formation, based on the analogy of an S–N–S junction with a non-superconducting Sm–N–Sm planar system.

In the past, semiclassical excitation spectra of bound states in inhomogeneous superconductors were compared to the spectra of electrons bound in a normal $U(x)$-potential square well (Saint-James 1964, Kulik 1969, Bardeen and Johnson 1972, Kümmel 1974). We want to present a similar analysis making use of the *exact* energy spectra presented in section 3.1. First, let us investigate physical characteristics of bound states associated with a single energy band.

Every state characterized by quantum numbers μ_t, ℓ and n can be interpreted as a mixture of particles and holes. We can estimate the weights of particle-like and hole-like components by evaluating the integrals

$$W_u = \int \mathrm{d}x \ |u(x)|^2 \qquad W_v = \int \mathrm{d}x \ |v(x)|^2. \tag{13}$$

Note that always $W_u + W_v = 1$ due to the normalization condition for bound states (de Gennes 1966). Evidently W_u is the probability that a particular excitation is a particle while W_v is the probability that it is a hole.

Another characteristic feature of an exponentially damped bound state is its penetration length D. For (μ_t,E)-points inside the A_{sup}-region, both functions of the fundamental system decay in the superconducting layers at $|x| > R$ with the same rate and, therefore, D clearly is (cf. equation (9))

$$D = \left[\frac{1}{\sqrt{2}} \sqrt{-\mu_t + \sqrt{{\mu_t}^2 + \Delta_0^2 - E^2}} \right]^{-1}. \tag{14}$$

For (μ_t,E)-points inside the B_{sup}-region, the two basis functions described by equation (7) decay with different rates, yielding actually two different penetration lengths. It is natural to consider the longer of them, which means that, inside the B_{sup}-region, we have

$$D = \left[\sqrt{-\left(\mu_t + \sqrt{E^2 - \Delta_0^2} \right)} \right]^{-1}. \tag{15}$$

Note that the penetration length D defined in this way diverges whenever the bound-states band merges into the continuum states region (cf. figure 2). Plausibly, this is because the state ceases to be bound at that point.

In figure 10, the 'probabilities' W_u and W_v (defined by equation (13)) together with the penetration length D (computed from equation (14)) are displayed in a limited μ_t-range for the lowest even-parity band (i.e. for the lowest of the bands presented in figures 3 and 5). The general tendencies illustrated by this figure are obeyed by all the bands as well: (i) parts of the $E_{\ell n}(\mu_t)$-curve with negative slopes correspond to predominantly *particle-like states*,

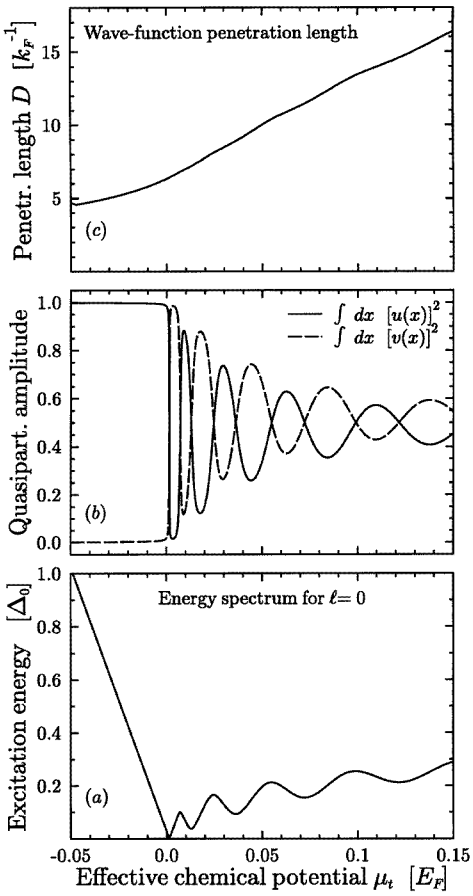

Figure 10. Physical characteristics of the band of $\ell = 0$ symmetry lowest in energy: the energy spectrum (*a*), integrals of the quasiparticle amplitudes W_u and W_v (*b*) and the length of penetration of the wave-function into the superconducting layer (*c*) are displayed within the same μ_t-range.

while parts of the $E_{\ell n}(\mu_t)$-curve with positive slopes correspond to *hole-like states*; (ii) the penetration length D increases with μ_t for $E < \Delta_0$ and decreases with μ_t for $E > \Delta_0$. When $\mu_t \to \mu$, both W_u and W_v approach 1/2, which means that the excitation is with an equal probability either a particle or a hole, similarly to in the case for $E = \Delta_0$ (see equation (8)). For negative μ_t, the excitation is almost exclusively a particle.

These findings are in agreement with the expectations based on a similar analysis made for spinor wave-functions of a *uniform superconductor*. Namely, considering the definition (4), the excitation spectrum of a homogeneous system can be expressed in terms of the μ_t-variable as

$$E_{k_x}(\mu_t) = \sqrt{(k_x^2 + k_y^2 + k_z^2 - \mu)^2 + \Delta_0^2} = \sqrt{(k_x^2 - \mu_t)^2 + \Delta_0^2} \tag{16}$$

and the BCS 'coherence factors' in case of a uniform medium are

$$u_h = \sqrt{\frac{1}{2}\left(1 + \frac{k_x^2 - \mu_t}{E}\right)} \qquad v_h = \sqrt{\frac{1}{2}\left(1 - \frac{k_x^2 - \mu_t}{E}\right)} \tag{17}$$

where $E_{k_x}(\mu_t)$ of equation (16) has been abbreviated to just E. Keeping k_x fixed, it is easy to show that when the excitation energy is decreasing with μ_t, i.e. when the slope of the $E_{k_x}(\mu_t)$-curve is negative, u_h is larger than v_h indicating the predominantly particle-like character of the excitation. On the other hand, when the slope of the $E_{k_x}(\mu_t)$-curve is positive, clearly $v_h > u_h$ and the excitation is mainly a hole.

In what now follows, we shall attempt to provide a simple physical picture of the above complex process of bound-states formation in an S–N–S junction. One way of looking at a superconductor is to stress its energy gap and to consider it a special case of a semiconductor. The superconducting gap is then interpreted as a *forbidden region* around the effective chemical potential μ_t. Electrons with single-particle energies close to μ_t then form bound states in the central normal-metal layer, because they cannot spread freely into the outer superconductor/semiconductor layers.

To analyse this picture quantitatively, an energy spectrum of an Sm–N–Sm junction (i.e. of a semiconducting analogy of the system depicted in figure 1) will be calculated. For a fixed effective chemical potential μ_t, it is necessary to investigate an auxiliary one-dimensional system as displayed in figure 11. If $\mu_t < 0$, this auxiliary system becomes just a one-dimensional square potential well (and hence does not change with μ_t any more). For a treatment of a similar problem of electron states in semiconducting heterostructures, the reader is referred to Dingle (1975).

For a given effective chemical potential μ_t, the one-electron energies ϵ within the $(\mu_t - \Delta_0; \mu_t + \Delta_0)$ interval form a discrete spectrum of bound states. States with one-electron energies ϵ above μ_t correspond to *particles*; their excitation energy E is

$$E = \epsilon - \mu_t. \tag{18}$$

Note that this relation is true for negative μ_t as well as for $\mu_t > 0$. States with one-electron energies ϵ below μ_t correspond to *holes* and their excitation energy E is

$$E = \mu_t - \epsilon. \tag{19}$$

Obviously, holes can exist only if $\mu_t > 0$.

Strictly speaking, it is not possible to describe our auxiliary system with a normal one-electron $U(x)$-potential: the 'potential well' in figure 11 extends just from $\mu_t - \Delta_0$ to $\mu_t + \Delta_0$ and the electrons can move freely below it. Nevertheless, it is possible to estimate what the excitation spectrum of this system would look like, employing concepts similar to those applied in semiconductor heterostructure studies (Dingle *et al* 1974, Dingle 1975, Döhler 1981).

Inside the normal region, i.e. for $|x| < R$, the one-electron wave-functions are

$$\begin{aligned} \psi_N(x) &= \cos(\gamma x) \Leftrightarrow \ell = 0 \qquad \text{(even states)} \\ \psi_N(x) &= \sin(\gamma x) \Leftrightarrow \ell = 1 \qquad \text{(odd states)} \end{aligned} \tag{20}$$

and the frequency γ is

$$\gamma = \sqrt{\epsilon}. \tag{21}$$

In the semiconducting regions, i.e. for $|x| > R$, the one-electron wave-functions are

$$\psi_S(x) = \exp(-\beta|x|) \tag{22}$$

and the damping factor β is determined by the 'distance' of the one-electron energy level ϵ from the relevant edge of the forbidden region,

$$\beta = \sqrt{\mu_t + \Delta_0 - \epsilon} \Leftrightarrow \epsilon \in \langle \mu_t; \mu_t + \Delta_0 \rangle \qquad \text{(particles)} \tag{23}$$

$$\beta = \sqrt{\epsilon - \mu_t + \Delta_0} \Leftrightarrow \epsilon \in \langle \mu_t - \Delta_0; \mu_t \rangle \qquad \text{(holes)}. \tag{24}$$

If $\mu_t < \Delta_0$, the equation (24) for holes ought to be replaced by

$$\beta = \sqrt{\epsilon}. \tag{25}$$

Matching the wave-functions and their derivatives at the interface provides the secular equation yielding the one-electron energies $\epsilon_{\ell n}(\mu_t)$. The excitation energies E are then evaluated relying on equations (18) and (19).

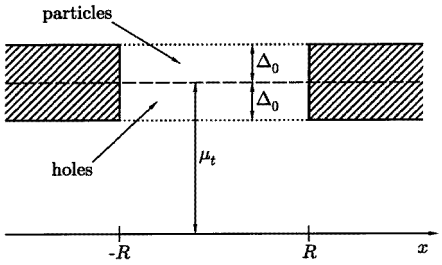

Figure 11. A schematic depiction of an auxiliary non-superconducting Sm–N–Sm system. The 'potential well' extends for $|x| > R$ from $\mu_t - \Delta_0$ to $\mu_t + \Delta_0$; the forbidden regions are shaded.

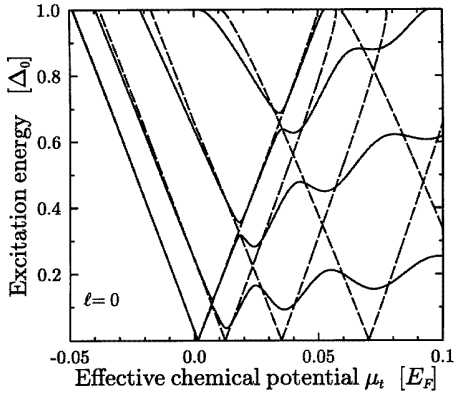

Figure 12. A comparison of energy bands of a superconducting S–N–S system (solid lines) and of a corresponding non-superconducting auxiliary Sm–N–Sm system (broken lines) for even-parity bound states ($\ell = 0$) for $-0.05E_F < \mu_t < 0.1E_F$.

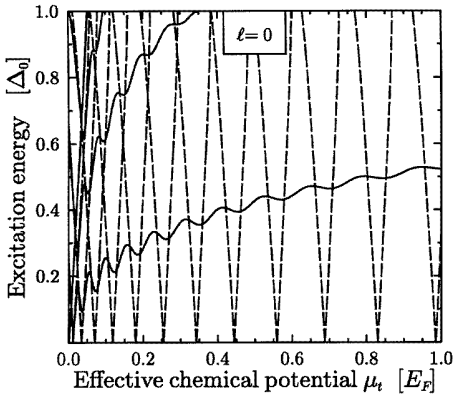

Figure 13. A comparison of energy bands of a superconducting S–N–S system (solid lines) and of a corresponding non-superconducting Sm–N–Sm system (broken lines) for even-parity bound states for $0 < \mu_t < \mu = 1.0E_F$.

The excitation spectrum of this auxiliary Sm–N–Sm system is compared with the exact spectrum for a proper S–N–S system in figures 12 and 13 for two ranges of μ_t. Dashed curves with negative slopes correspond to particles in the Sm–N–Sm junction; dashed curves with positive slopes correspond to holes (cf. figure 10). Only results for $\ell = 0$ are presented; analogous plots for the other symmetry reveal the same qualitative features.

Let us summarize the basic trends. (i) When one concentrates on comparing particle-like and hole-like sections of the energy bands separately, excitation spectra of the two systems are quite similar for small μ_t. This similarity improves when E or μ_t decreases. (ii) The most striking difference is the absence of 'minigaps' between adjacent bands for the auxiliary system: particle-like and hole-like bands of the Sm–N–Sm structure cross

each other in places where the energy gap seems to be restored in the S–N–S junction. (iii) For large μ_t, the energy bands of the Sm–N–Sm system do not resemble those of a superconducting S–N–S junction. However, for both systems, the numbers of particle-like and hole-like branches of the excitation spectra still agree.

The following interpretation of the excitation spectra of S–N–S junctions has therefore been reached: basically, the bound states are 'trapped' inside the middle normal region by the same mechanism which determines electronic structure of semiconducting heterostructures, i.e. the electrons concerned cannot penetrate deep into the superconducting regions because there are no allowed states available for them. The superconductivity of the outer layers manifests itself through restoring energy 'minigaps': wherever particle-like and hole-like bands cross in the (μ_t,E)-plane, excitations with opposite $k_y + k_z$ occur (see equation (4)), making the BCS pairing of quasiparticles with opposite momenta possible (de Gennes 1966). When the penetration length of the excitations into the superconducting region increases, the effect of superconductivity is enhanced and the minigaps eventually get larger, as is observed for large μ_t in figure 13.

Although this interpretation is based on investigation of an S–N–S planar junction, we believe that it is relevant to other geometries as well, because excitation spectra of bound states of cylindrical geometry (e.g. a vortex in a mixed state of a type-II superconductor) exhibit the same basic features as those displayed in this paper in figures 3–6 (Šipr and Györffy 1992).

4. Density of states

So far, only the energy spectra $E_{\ell n}(\mu_t)$ have been investigated. However, a quantity which is directly related to observation is rather the density of states (DOS). Two types of local quasiparticle densities of states can be distinguished, namely a local particle-like DOS $n_u(x, E)$,

$$n_u(x, E) = -\frac{1}{\pi}\operatorname{Im} G_{uu}(x, x; E) = \sum_n |u_n(x)|^2\, \delta(E - E_n) \tag{26}$$

and a local hole-like DOS $n_v(x, E)$,

$$n_v(x, E) = -\frac{1}{\pi}\operatorname{Im} G_{vv}(x, x; E) = \sum_n |v_n(x)|^2\, \delta(E - E_n). \tag{27}$$

In these definitions, $G_{uu}(x, x'; E)$ and $G_{vv}(x, x'; E)$ are diagonal components of a 2×2-matrix Green function appropriate to BdG equations (1) and n stands for all possible quantum states with $E_n > 0$.

For the bound states investigated in this paper, equations (26) and (27) can be transformed to

$$n_w(x, E) = \frac{1}{4\pi} \sum_\ell \sum_{\mu_E} \left| \left(\frac{\partial E_q(\mu_t)}{\partial \mu_t} \right)_{\mu_t = \mu_E} \right|^{-1} |w_{\mu_E q}(x)|^2 \tag{28}$$

where w is either u or v, ℓ is the parity, q abbreviates all quantum numbers except for μ_t, and μ_E is such a value of μ_t that $E_q(\mu_E) = E$. The occurrence of the reciprocal value of the differentiation of the spectral curve $E_q(\mu_t)$ in equation (28) means that the densities of states will have a fine and complicated structure, containing possibly a large number of singularities (cf. plots of $E_q(\mu_t)$-curves in figures 3–6). To get physically relevant information, smoothing is necessary. To give a rough idea of the effect of such a smoothing, we display a raw untreated local particle-like DOS for $x = 0$ together with a smoothed curve

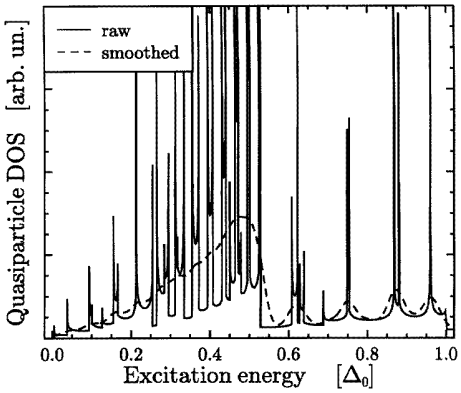

Figure 14. The local particle-like quasiparticle density of states $n_u(x, E)$ in an S–N–S system at $x = 0$: the raw untreated result (solid line) together with a smoothed curve obtained by convoluting the former with a Gaussian curve (broken line).

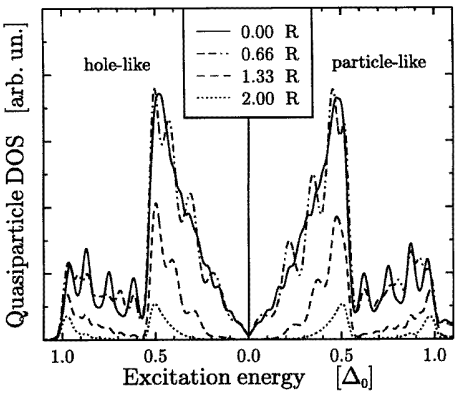

Figure 15. Smoothed local hole-like (the left-hand half of the graph) and particle-like (the right-hand half of the graph) quasiparticle densities of states in an S–N–S system for four choices of the distance x from the centre of the middle normal region.

in figure 14. The smoothing was done by convoluting the original spectrum of equation (28) with a Gaussian curve of a full width at half-maximum equal to $0.002E_F$ (which is $0.04\Delta_0$ for our system defined by (10)).

The dependences of local densities of bound states on the x-coordinate are investigated in figure 15, where both smoothed $n_u(x, E)$ and smoothed $n_v(x, E)$ are shown for four choices of x. As is to be expected, local densities of bound states decrease as we are moving away from the middle, normal, layer. An interesting feature is that the main peak at $E \simeq 0.5\Delta_0$ decreases with x more quickly then the shoulder at $E \simeq 0.95\Delta_0$. The position of the smoothed main peak remains *fixed* when x varies. This is in agreement with previous semiclassical calculations for the same geometry (Tanaka and Tsukada 1991, Tanaka *et al* 1991). Interestingly, calculations of the density of bound states in a *vortex core* indicate, in contrast, a strong dependence of the position of the main peak in the local DOS on the radial distance r (Shore *et al* 1989, Klein 1990).

Note that particle-like and hole-like densities are similar but not identical. The most striking difference occurs for $E > \Delta_0$—there are hardly any holes above the gap left, in contrast to what is found in the case of the finite particle-like DOS at those energies. This is in agreement with the finding of section 3.3 that states above Δ_0 are mainly particles.

In section 3.2, exact energy bands were compared to those obtained within the semiclassical approximation. To estimate observable implications of the differences, it is instructive to compare corresponding densities of states. The semiclassical analysis of Plehn *et al* (1991) is based on the following simple analytical expression for the combined x-integrated density of states:

$$g(E) = \int_{-\infty}^{\infty} \mathrm{d}x \, [n_u(x, E) + n_v(x, E)] \,. \tag{29}$$

Considering equations (29), (28) and the normalization condition for bound states, we find a formal expression for $g(E)$:

$$g(E) = \frac{1}{4\pi} \sum_{\ell} \sum_{\mu_E} \left| \left(\frac{\partial E_q(\mu_t)}{\partial \mu_t} \right)_{\mu_t = \mu_E} \right|^{-1} . \tag{30}$$

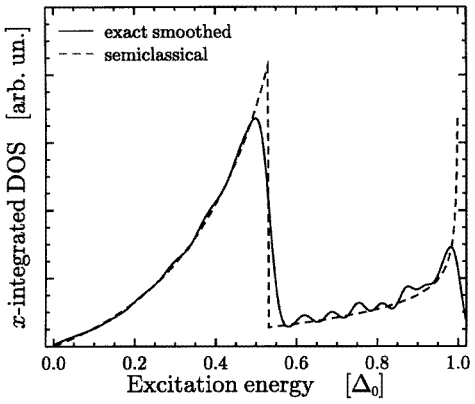

Figure 16. A comparison of the x-integrated combined densities of states $g(E)$ in an S–N–S system: a smoothed curve calculated using exact solutions (solid line) together with a curve obtained within the semiclassical approximation (broken line).

A comparison of the combined x-integrated DOS calculated using exact solutions of BdG equations (equation (30) of this paper) and using solutions obtained within the semiclassical approximation (equation (20) in Plehn *et al* (1991)) is presented in figure 16 for the system parameters of equation (10).

It is evident that the semiclassical result does not differ significantly from the exact one. Rapid oscillations of the smoothed exact curve persist only above the main peak, for energies $0.6\Delta_0 < E < \Delta_0$. Otherwise, there seems to be a little chance to observe any deviations from the semiclassical prediction experimentally. Note also that the *difference* between the 'semiclassical DOS' and the DOS calculated from exact solutions *is large* if the number of energy bands below the gap is small: in that case, namely, the singularities in the DOS caused by the zero $(\partial E_q(\mu_t)/\partial\mu_t)$-differentiation are far apart and hence not smeared out in the process of DOS broadening (cf. figures 3–8 and 14 and equations (28) and (30)). This implies that the fine DOS structure predicted on the strength of using the exact solutions of BdG equations could be observed in systems with a small gap Δ_0 or with a small thickness of the normal layer $2R$, in accordance with the finding mentioned at the end of section 3.1. One has to bear in mind, however, that the effect discussed in this section might be obscured in real S–N–S structures by other effects not described by our simple 'jellium' model (such as the band structure of the materials involved). A quantitative assessment of such effects would go far beyond the scope of this paper, however.

A novel feature of our study is the inclusion of bound states *above* the gap, which appear for negative μ_t only. In section 3.3, it was found that the analogy between an S–N–S junction (described by figure 1) and an Sm–N–Sm junction (shown in figure 11) works particularly well for $\mu_t < 0$ (see figure 12). To investigate the analogy a bit more deeply, we compare densities of states in an S–N–S junction, calculated from equations (26) and (30), with the same quantities calculated for a non-superconducting Sm–N–Sm system for $E > \Delta_0$.

The raw (unsmoothed) quasiparticle local DOS $n_u(x, E)$ for $x = 0$ is displayed in figure 17 for both S–N–S and Sm–N–Sm systems, and the combined x-integrated DOS $g(E)$ is shown in figure 18. It can be seen immediately that the two curves to be compared closely resemble each other, especially in the case of the combined x-integrated DOS $g(E)$, where they can hardly be distinguished one from another for $E > 2\Delta_0$. This fact supports

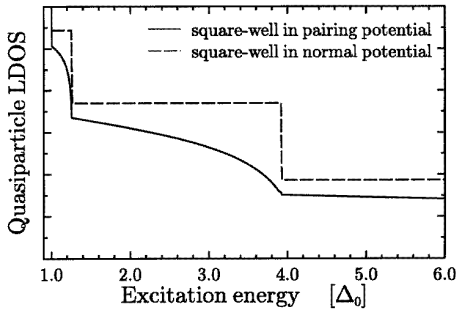

Figure 17. The local particle-like quasiparticle DOS $n_u(x, E)$ in an S–N–S system (solid line) together with the local quasiparticle DOS for a square well in a normal $U(x)$-potential (broken line) for energies above the gap. Both curves have been calculated for $x = 0$.

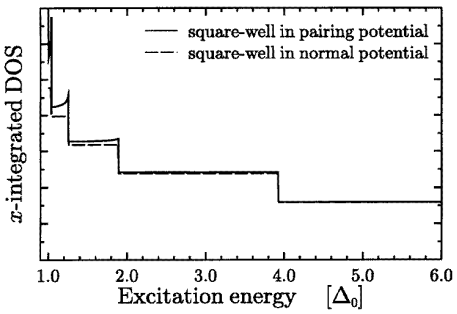

Figure 18. The x-integrated combined DOS $g(E)$ in an S–N–S system (solid line) together with the x-integrated combined DOS for a square well in a normal $U(x)$-potential (broken line) for energies above the gap.

the interpretation of bound states proposed in section 3.3 in this particular energy range. (On the other hand, one cannot expect good agreement between densities of states for the Sm–N–Sm and S–N–S systems if the energy E is below the gap, as in that case states with large μ_t, for which their energy spectra differ significantly, become important—see figure 13.)

It is necessary to note that, although conceptually bound states above the gap pose a significant feature, their contribution to the quasiparticle DOS above the gap is very small in comparison with the contribution of extended states in that energy region (cf. calculated DOS curves in figure 2 of Plehn *et al* (1991) or in figure 2*a* of Furusaki and Tsukada (1991)). Hence, it would be extremely difficult to identify the contribution of the bound states above the gap relying on DOS measurements in real systems.

5. Scattering of quasiparticles at N–S interfaces

In section 3.3, we gave an *intuitive* interpretation of the mechanism of formation of bound states in S–N–S junctions. We also noted that it is conventional to regard Andreev reflection as the key to understand the trapping of quasiparticles inside the normal regions embedded in a superconductor (Abrikosov 1988). In this section, we intend to present a thorough analysis of scattering processes at N–S (normal-metal–superconductor) interfaces, taking the parallel-to-the-interface degree of freedom fully into account. In that respect, our analysis is a supplement to that of Blonder *et al* (1982), who limited their investigation to a proper one-dimensional case only.

5.1. Basic considerations

Suppose we are investigating a system composed of a semi-infinite normal metal for $x < 0$ and of a semi-infinite superconductor with a uniform pairing potential $\Delta(x) = \Delta_0$ for $x > 0$. The normal $U(x)$-potential is zero everywhere. We want to investigate the scattering of an electron by the N–S interface. Quasiparticles are labelled by their excitation energy E and by the effective chemical potential μ_t (see equation (4)). In three dimensions, the incident

electron is described by (Kümmel 1969, Blonder *et al* 1982)

$$\hat{\psi}_{\text{inc}} = \begin{pmatrix} 1 \\ 0 \end{pmatrix} \exp(\mathrm{i}\gamma_1 x) \exp[\mathrm{i}(k_y y + k_z z)]. \tag{31}$$

The frequency γ_1 is defined by equation (6); the Y- and Z-directions are 'factored-out' similarly to in equation (2). Recalling figure 2(a) and the discussion at the end of section 2, it can be seen that such an incoming electron wave can occur only in regions C_{norm} and D_{norm}. When this incoming electron interacts with the N–S interface, it is subjected (with various probabilities) to four distinct processes (Blonder *et al* 1982): normal reflection, Andreev reflection, normal transmission (called transmission 'without branch crossing' in Blonder *et al* (1982)) and Andreev transmission ('with branch crossing') (see also Kümmel (1969) for a thorough discussion of group velocities of quasiparticles in the situation concerned). Depending on the position in the (μ_t, E)-plane in figure 2, the outgoing quasiparticles either propagate to infinity or are exponentially damped.

A normally reflected wave

$$\hat{\psi}_R^{\text{norm}} = \begin{pmatrix} 1 \\ 0 \end{pmatrix} \exp(-\mathrm{i}\gamma_1 x) \exp[\mathrm{i}(k_y y + k_z z)] \tag{32}$$

can propagate inside C_{norm}- and D_{norm}-regions—i.e. under the same conditions as the incident wave can. On the other hand, Andreev reflection

$$\hat{\psi}_R^{\text{And}} = \begin{pmatrix} 0 \\ 1 \end{pmatrix} \exp(\mathrm{i}\gamma_2 x) \exp[\mathrm{i}(k_y y + k_z z)] \tag{33}$$

occurs only in the D_{norm}-region of the (μ_t, E)-plane; elsewhere it has to be substituted for with a function exponentially damped inside the normal metal.

No kind of transmission into the superconducting region is possible for $E > \Delta_0$, i.e. inside the A_{sup}-region. Similarly, neither it is possible within the B_{sup}-region (see figure 2(b)). Normal transmission giving rise to the wave-function

$$\hat{\psi}_T^{\text{norm}} = \begin{pmatrix} u_0 \\ v_0 \end{pmatrix} \exp(\mathrm{i}\omega_1 x) \exp[\mathrm{i}(k_y y + k_z z)] \tag{34}$$

can exist in the C_{sup}- and D_{sup}-regions. An Andreev-transmitted wave

$$\hat{\psi}_T^{\text{And}} = \begin{pmatrix} v_0 \\ u_0 \end{pmatrix} \exp(-\mathrm{i}\omega_2 x) \exp[\mathrm{i}(k_y y + k_z z)] \tag{35}$$

can propagate only if the corresponding (μ_t, E)-point is inside the D_{sup}-region. The frequencies γ_2, ω_1 and ω_2 are defined in equations (6) and (9), coherence factors u_0, v_0 by equation (8).

With each of the wave-functions (31)–(35), a probability current $\boldsymbol{j}$ can be associated, using the relation (Kümmel 1969, Blonder *et al* 1982)

$$\boldsymbol{j} = 2\,\mathrm{Im}\,[u^* \boldsymbol{\nabla} u - v^* \boldsymbol{\nabla} v]. \tag{36}$$

One can find easily that the x-component (perpendicular to the interface) of the probability current is positive for $\boldsymbol{j}_{\text{inc}}$, $\boldsymbol{j}_T^{\text{norm}}$ and $\boldsymbol{j}_T^{\text{And}}$ while it is negative for $\boldsymbol{j}_R^{\text{norm}}$ and $\boldsymbol{j}_R^{\text{And}}$. This indicates that the wave-functions (32) and (33) really correspond to reflected quasiparticles while the wave-functions (34) and (35) correspond to transmitted ones. The parallel-to-the-interface component of the current $\boldsymbol{j}$ always has the same sign for $\boldsymbol{j}_{\text{inc}}$, $\boldsymbol{j}_R^{\text{norm}}$ and $\boldsymbol{j}_T^{\text{norm}}$ while it has the opposite sign for $\boldsymbol{j}_R^{\text{And}}$ and $\boldsymbol{j}_T^{\text{And}}$. This reflects an interesting feature of the Andreev scattering, viz. that the tangential component of the current does change the sign, in contrast to what occurs in the case of the normal reflection or transmission (for an Andreev

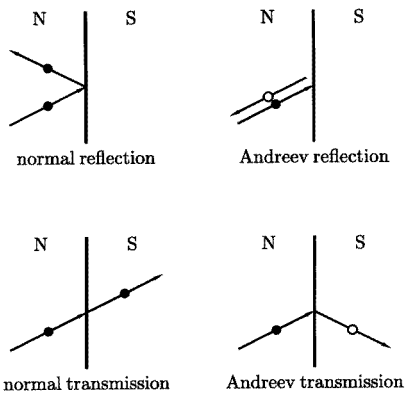

Figure 19. Changes in the direction of the probability current $\boldsymbol{j}$ in various scattering events at the N–S interface (schematic). An arrow with a full dot represents an excitation which is predominantly a particle; an arrow with a blank circle represents a hole-like excitation.

reflection, this was noted already by Andreev (1964)). Schematically, the changes in the direction of the current $\boldsymbol{j}$ in the four processes concerned in a proper three-dimensional case are depicted in figure 19.

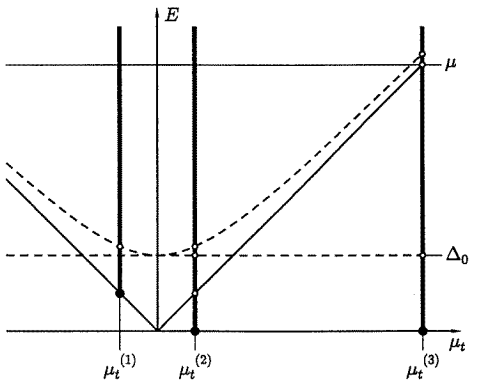

Figure 20. A schematic depiction of the three particular choices of the effective chemical potential μ_t for which the scattering at N–S interfaces is investigated in figures 21–25. For each μ_t, the beginning of the allowed range of energies E is marked by a full solid circle while sections of different scattering regimes are separated by empty circles (see the text for further details). The division of the (μ_t,E)-plane into individual regions, as suggested by thin solid and broken lines, is the same as in figure 2.

In order to calculate probabilities of the scattering processes investigated, first it is necessary to match the wave-functions and their derivatives in the normal region,

$$\hat{\psi}_{\mathrm{inc}} + a\hat{\psi}_R^{\mathrm{norm}} + b\hat{\psi}_R^{\mathrm{And}}$$

and in the superconducting region

$$c\hat{\psi}_T^{\mathrm{norm}} + d\hat{\psi}_T^{\mathrm{And}}$$

at $x = 0$ and to calculate the matching coefficients a, b, c and d. If any of the propagating solutions presented in equations (33)–(35) does not exist, it has to be substituted for with a

corresponding *exponentially damped* solution. When the matching coefficients a, b, c and d are available, it is possible to calculate the x-components of the probability currents $\boldsymbol{j}_{\rm inc}$, $\boldsymbol{j}_R^{\rm norm}$, $\boldsymbol{j}_R^{\rm And}$, $\boldsymbol{j}_T^{\rm norm}$ and $\boldsymbol{j}_T^{\rm And}$ associated with the wave-functions presented in equations (31)–(35). If no solution of a given type propagating in the X-direction exists, the x-component of the corresponding current $\boldsymbol{j}$ is naturally zero. Finally, the probability of any of the scattering processes is obtained on dividing the the x-components of the relevant probability currents by the x-component of $\boldsymbol{j}_{\rm inc}$ (Blonder *et al* 1982, Yamamoto *et al* 1991).

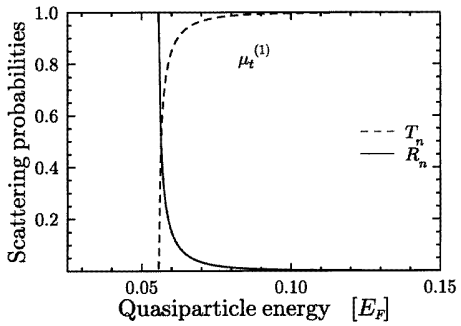

Figure 21. Probabilities of normal reflection $R_{\rm n}$ (solid line) and normal transmission $T_{\rm n}$ (broken line) of an electron at an N–S interface for $\mu_t = \mu_t^{(1)}$. Andreev reflection and Andreev transmission are identically zero for any E for this choice of μ_t.

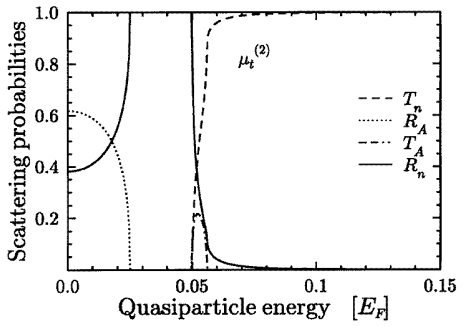

Figure 22. Probabilities of normal reflection $R_{\rm n}$ (solid line), normal transmission $T_{\rm n}$ (broken line), Andreev reflection $R_{\rm A}$ (dotted line) and Andreev transmission $T_{\rm A}$ (chain line) of an electron at an N–S interface for $\mu_t = \mu_t^{(2)}$.

In this paper, we want to investigate the energy dependence of the probabilities of normal reflection $R_{\rm n}$, Andreev reflection $R_{\rm A}$, normal transmission $T_{\rm n}$ and Andreev transmission $T_{\rm A}$. Employing different values of the effective chemical potential μ_t, we will be able to distinguish cases in which only some of the scattering processes are permitted, the others having identically zero probability. Three different generic situations are depicted in figure 20 (cf. also figure 2). For example, for $\mu = \mu_t^{(1)}$, just two distinct 'phases' are possible: (i) $R_{\rm n} \neq 0$, $R_{\rm A} = T_{\rm n} = T_{\rm A} = 0$ if the (μ_t, E)-point falls in the $A_{\rm sup}$-region or in the $B_{\rm sup}$-region; and (ii) $R_{\rm n} \neq 0$, $T_{\rm n} \neq 0$, $R_{\rm A} = T_{\rm A} = 0$ if (μ_t, E) is in the $C_{\rm sup}$-region. Similar phases can be identified for $\mu_t = \mu_t^{(2)}$ and $\mu_t = \mu_t^{(3)}$ as well.

The *one-dimensional situation* studied by Blonder *et al* (1982) belongs particularly to the $\mu_t = \mu_t^{(3)}$-class (in one dimension, obviously $\mu_t = \mu$—cf. equation (4)). However, although Blonder *et al* (1982) went beyond the semiclassical approximation, their results are still only approximate ones (see the appendix of their paper). Thus it might be useful to see how much their conclusions change when exact calculation is employed.

5.2. Particular results

The results for each of the specific cases, $\mu_t^{(1)} = -0.5\Delta_0$, $\mu_t^{(2)} = 0.5\Delta_0$ and $\mu_t^{(3)} = \mu$, are displayed in figures 21–25. Similarly to the choice presented in equation (10), we put $\Delta_0 = 0.05E_{\rm F}$, $\mu = 1.0E_{\rm F}$ throughout this section. The simplest case of all, $\mu_t = \mu_t^{(1)}$, is studied in figure 21. The N–S interface is totally reflective for $E < \sqrt{((\mu_t^{(1)})^2 + \Delta_0^2)}$; then the reflection probability $R_{\rm n}$ decreases rapidly, implying a steep rise of $T_{\rm n}$ (as the natural condition

$$R_{\rm n} + R_{\rm A} + T_{\rm n} + T_{\rm A} = 1$$

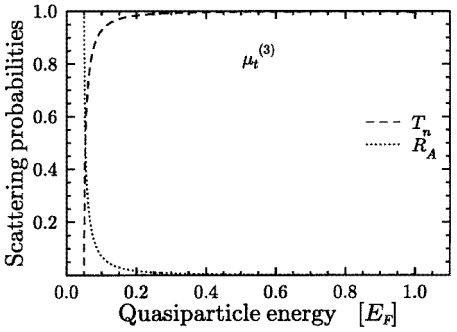

Figure 23. Probabilities of normal transmission $T_{\rm n}$ (broken line) and Andreev reflection $R_{\rm A}$ (dotted line) of an electron at an N–S interface for $\mu_t = \mu_t^{(3)}$. Normal reflection $R_{\rm n}$ and Andreev transmission $T_{\rm A}$ are too small to be visible with this y-axis scale.

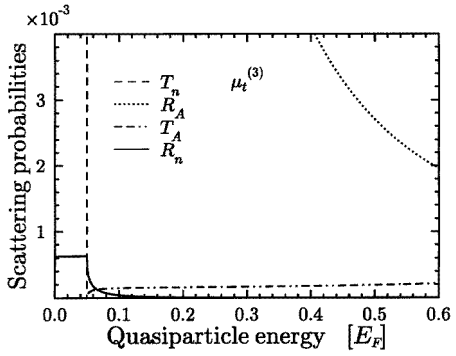

Figure 24. Probabilities of normal reflection $R_{\rm n}$ (solid line), normal transmission $T_{\rm n}$ (broken line), Andreev reflection $R_{\rm A}$ (dotted line) and Andreev transmission $T_{\rm A}$ (chain line) of an electron at an N–S interface for $\mu_t = \mu_t^{(3)}$. Note the changed scaling of the y-axis with respect to that of figure 23.

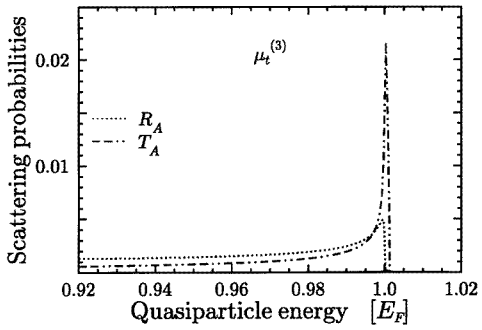

Figure 25. Probabilities of Andreev transmission $T_{\rm A}$ (chain line) and Andreev reflection $R_{\rm A}$ (dotted line) of an electron at an N–S interface for $\mu_t = \mu_t^{(3)}$. Normal reflection $R_{\rm n}$ is too small to be visible in this scale, and normal transmission $T_{\rm n}$ is beyond the range of the y-axis of this plot (cf. figure 23).

holds).

The situation for $\mu_t = \mu_t^{(2)}$ is analysed in figure 22. The overall picture is a rather more complicated one than in figure 21. For $E < \Delta_0$, the transmission probabilities $T_{\rm n}$ and $T_{\rm A}$ are zero identically. If $E < \Delta_0/2$, both normal and Andreev reflection are possible—figure 22 demonstrates that the regime of dominant Andreev reflection is gradually switched to the situation when $R_{\rm n} < R_{\rm A}$. Only one type of scattering process, viz. a normal reflection, is possible for $\Delta_0/2 < E < \Delta_0$. Transmission processes become available for $E > \Delta_0$: Andreev transmission occurs only for energies between $\Delta_0/2$ and $\sqrt{((\mu_t^{(2)})^2 + \Delta_0^2)}$ (cf. figure 20), while normal transmission is possible for any $E > \Delta_0$. Similarly to what is seen in figure 21, the transmission probability $T_{\rm n}$ soon becomes larger than $R_{\rm n}$ by an order of magnitude.

In figures 23–25, the case where $\mu_t = \mu_t^{(3)}$ is investigated. The overall situation (figure 23) seems to confirm approximative results of Blonder *et al* (1982) (cf. figure 5 for $Z = 0$ in their paper): Andreev reflection dominates for $E < \Delta_0$, then normal transmission

becomes possible and soon becomes the dominant process. Other processes (neglected by Blonder *et al* (1982)) contribute as well; however, their probability is smaller by an order of magnitude. This is demonstrated in figures 24 and 25 (note the different scales on the vertical axes of these figures). The normal reflection, although in principle permitted throughout the energy range, practically vanishes for $E > \Delta_0$. The Andreev transmission starts to rise very slowly from $T_A = 0$ at $E = \Delta_0$ and reaches its peak value close to $E = \sqrt{((\mu_t^{(3)})^2 + \Delta_0^2)}$, which is the upper limit of its domain of definition. Interestingly, Andreev reflection also has a local maximum just before the upper limit of its domain of definition: $E = \mu_t^{(3)}$ (figure 25). We have found that these features are generic to any μ_t between $\mu_t = \Delta_0$ and $\mu_t = \mu$. However, the absolute heights of these local maxima of R_A and T_A decrease with increasing μ_t.

5.3. Discussion

The results given in section 5.2 demonstrate that, when a proper *three-dimensional case* is investigated, the manifold of scattering processes at the N–S interface is more diversified than might be inferred from the one-dimensional study of Blonder *et al* (1982). In particular, this is true even in absence of any $U(x)$-potential steps (or barrier-simulating $\delta(x)$-type potentials).

For a one-dimensional model, the approximations employed by Blonder *et al* (1982) do not lead to essential changes with respect to an exact calculation: the differences between the overall picture presented in figures 23–25 of this paper on the one hand and the $Z = 0$ subsection of figure 5 in Blonder *et al* (1982) on the other are very small in magnitude and would be difficult to detect experimentally in real superconductors.

Now, let us turn back to the problem of interpretation of bound states in S–N–S junctions. The general analysis of quasiparticle scattering at N–S junctions together with particular results shown in section 5.2 indicate that the often-quoted statement that 'bound states in S–N–S junctions are formed by Andreev reflection' is not entirely true, as pointed out already by Kümmel (1974). *Andreev reflection* is limited just to situations where $\mu_t > E$ (cf. figures 2 and 20 and section 5.1). For $\mu_t < 0$ or for $\mu_t < E$, a *normal* reflection is the only process responsible for binding quasiparticles inside the middle normal region. Physically, such states describe quasiparticles moving rapidly in the direction parallel to the N–S interface.

Apart from that, whenever Andreev reflection is possible, normal reflection occurs as well. To investigate the gradual changeover from a normal-reflection-dominated situation to an Andreev-reflection-dominated situation, the integrals

$$S_{\text{norm}} = \frac{1}{\Delta_0} \int_0^{\Delta_0} \mathrm{d}E \; R_n(E) \tag{37}$$

and

$$S_{\text{And}} = \frac{1}{\Delta_0} \int_0^{\Delta_0} \mathrm{d}E \; R_A(E) \tag{38}$$

were computed. The results for $\Delta_0 = 0.05E_F$ and $\mu = 1.0E_F$ are displayed in figure 26. It is interesting to note that the μ_t-range where the normal reflection is significant (approximately $\mu_t < 2\Delta_0$) is more or less identical to the range where Sm–N–Sm energy bands agree with S–N–S energy bands (cf. figure 12).

Results similar to those presented in this section were obtained by Hurd and Wendin (1994) who studied a one-dimensional version of our system (cf. figure 1), with different

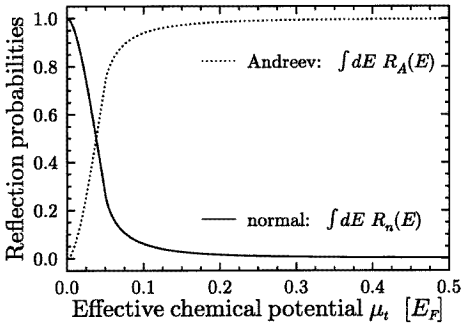

Figure 26. Integrated probabilities of the normal reflection S_{norm} (solid line) and of the Andreev reflection S_{And} (dotted line) of an electron at an N–S interface.

phases ϕ_L, ϕ_R of the complex pairing potential $\Delta(x)$ in the left- and right-hand-side superconductors. They found that disposing of the semiclassical approximation leads to coexistence of the normal reflection of quasiparticles at the N–S interface alongside the Andreev one.

The last remark concerns the fact that, in section 3.1, we have not found any bound states for $\mu_t < -E$, i.e. in the B_{norm}-region of the (μ_t,E)-plane. As already discussed in section 5.1, no propagating particle can exist with such parameters. Hence, no standing waves can form for such (μ_t,E)-values at all in the normal layer, implying that no 'conventional' bound states are able to exist in the B_{norm}-region. The only remaining choices would be purely interface-related states. Although we have not proven it rigorously, our experience indicates that this does not happen.

6. Conclusions

We have investigated excitation spectra of S–N–S junctions and scattering processes at N–S interfaces using exact solutions of the Bogoliubov–de Gennes equations. Our calculations demonstrate that whilst the semiclassical approximation accounts correctly for the overall trends of the $E_{\ell n}(\mu_t)$ spectral curves, it fails to describe some important details, especially for low values of the effective chemical potential $\mu_t = \mu - \left(k_y^2 + k_z^2\right)$. As might be expected, such differences as exist between the exact and semiclassical solutions are less pronounced in the case of the density of states and other integrated quantities.

As a new result, we have shown that bound states exist also for excitation energies above the gap Δ_0. These states correspond to low μ_t, i.e. to large parallel-to-the-interface momenta, and cannot altogether be accounted for within the semiclassical approximation.

Analysing the bound states in S–N–S junctions we have found that they can be well described with the help of an analogy with non-superconducting Sm–N–Sm junctions. The main effect of superconductivity on the bound states consists in opening energy minigaps wherever Sm–N–Sm hole-like and particle-like excitation energy bands cross and hybridize.

Finally we demonstrated that whilst the Andreev reflection is the dominant mechanism in trapping the bound states, it is not the only one. The normal reflection contributes as well and, for low μ_t, its importance increases. For states with $\mu_t < E$, the Andreev reflection is zero and the normal reflection becomes the only phenomenon responsible for generation of bound states in S–N–S junctions.

In conclusion we wish to stress that the key ideas outlined in this paper for a planar

geometry are most likely to be valid for other geometries as well. In particular they may be helpful in discussing bound states in the cylindrical vortices of type-II superconductors.

Acknowledgments

This work was partly supported by the British SERC (grant G/48381). One of the authors (OŠ) gratefully acknowledges a travel grant from The Royal Society, awarded under the agreement between The Royal Society and the Academy of Sciences of the Czech Republic.

References

Abrikosov A A 1988 *Fundamentals of the Theory of Metals* (Amsterdam: North-Holland)
Andreev A F 1964 *Sov. Phys.–JETP* **19** 1228
—— 1966 *Sov. Phys.–JETP* **22** 455
Ashida M, Aoyama S, Hara J and Nagai K 1989 *Phys. Rev.* B **40** 8673
Bardeen J and Johnson J L 1972 *Phys. Rev.* B **5** 72
Bardeen J, Kümmel R, Jacobs A E and Tewordt L 1969 *Phys. Rev.* **187** 556
Bar-Sagi J and Kuper C G 1974 *J. Low Temp. Phys.* **16** 73
Blonder G E, Tinkham M and Klapwijk T M 1982 *Phys. Rev.* B **25** 4515
Butler 1976 *Phys. Rev.* B **14** 468
Caroli C, de Gennes P G and Matricon J 1964 *Phys. Lett.* **9** 307
de Gennes P G 1966 *Superconductivity of Metals and Alloys* (New York: Benjamin)
de Gennes P G and Saint-James D 1963 *Phys. Lett.* **4** 151
Dingle R 1975 *Festkörperprobleme XV* ed H J Queisser (Braunschweig: Vieweg) p 21
Dingle R, Wiegmann W and Henry C H 1974 *Phys. Rev. Lett.* **33** 827
Döhler G H 1981 *Phys. Scr.* **24** 430
Entin-Wohlmann O and Bar-Sagi J 1978 *Phys. Rev.* B **18** 3174
Furusaki A and Tsukada M 1991 *Phys. Rev.* B **43** 10 164
Gunsenheimer U, Schüssler U and Kümmel R 1994 *Phys. Rev.* B **49** 6111
Gygi F and Schlüter M 1991 *Phys. Rev.* B **43** 7609
Hara J, Ashida M and Nagai K 1993 *Phys. Rev.* B **47** 11 263
Hurd M and Wendin G 1994 *Phys. Rev.* B **49** 15 258
Klein U 1990 *Phys. Rev.* B **41** 4819
Kobes R L and Whitehead J P 1987 *Phys. Rev.* B **36** 121
Kulik I O 1969 *Sov. Phys.–JETP* **28** 461
Kümmel R 1969 *Z. Phys.* **218** 472
—— 1974 *Phys. Rev.* B **10** 2812
—— 1977 *Phys. Rev.* B **16** 1979
Levi Yeyati A, Martín-Rodero A and Garcia-Vidal F J 1995 *Phys. Rev.* B **51** 3743
Martín-Rodero A, Garcia-Vidal F J and Levy Yeyati A 1994 *Phys. Rev. Lett.* **72** 554
Plehn H, Gunsenheimer U and Kümmel R 1991 *J. Low Temp. Phys.* **83** 71
Plehn H, Wacker O-J and Kümmel R 1994 *Phys. Rev.* B **49** 12 140
Saint-James D 1964 *J. Physique* **25** 899
Shore J, Huang M, Dorsey A and Sethna P 1989 *Phys. Rev. Lett.* **62** 3089
Šipr O and Györffy B L 1992 unpublished
Tanaka Y and Tsukada M 1991 *Solid State Commun.* **77** 593
Tanaka Y, Yamagami H and Tsukada M 1991 *Solid State Commun.* **79** 349
Yamamoto T, Suzuki H, Usuki T, Yoshisato Y and Nakano S 1991 *Japan. J. Appl. Phys.* **30** 3911